


Article

Entangling Lattice-Trapped Bosons with a Free Impurity: Impact on Stationary and Dynamical Properties

Maxim Pyzh ¹, Kevin Keiler ¹, Simeon I. Mistakidis ¹ and Peter Schmelcher ^{1,2,*}

¹ Center for Optical Quantum Technologies, Department of Physics, University of Hamburg, Luruper Chaussee 149, 22761 Hamburg, Germany; mpyzh@physnet.uni-hamburg.de (M.P.); kkeiler@physnet.uni-hamburg.de (K.K.); smistaki@physnet.uni-hamburg.de (S.I.M.)

² The Hamburg Centre for Ultrafast Imaging, Universität Hamburg, Luruper Chaussee 149, 22761 Hamburg, Germany

* Correspondence: mpyzh@physnet.uni-hamburg.de

Abstract: We address the interplay of few lattice trapped bosons interacting with an impurity atom in a box potential. For the ground state, a classification is performed based on the fidelity allowing to quantify the susceptibility of the composite system to structural changes due to the intercomponent coupling. We analyze the overall response at the many-body level and contrast it to the single-particle level. By inspecting different entropy measures we capture the degree of entanglement and intraspecies correlations for a wide range of intra- and intercomponent interactions and lattice depths. We also spatially resolve the imprint of the entanglement on the one- and two-body density distributions showcasing that it accelerates the phase separation process or acts against spatial localization for repulsive and attractive intercomponent interactions, respectively. The many-body effects on the tunneling dynamics of the individual components, resulting from their counterflow, are also discussed. The tunneling period of the impurity is very sensitive to the value of the impurity-medium coupling due to its effective dressing by the few-body medium. Our work provides implications for engineering localized structures in correlated impurity settings using species selective optical potentials.

Keywords: multi-layer multi-configuration time-dependent Hartree method (ML-MCTDHB); mixtures; impurity; fidelity; entanglement; von Neumann entropy; reduced densities; few-body dynamics



Citation: Pyzh, M.; Keiler, K.; Mistakidis, S.I.; Schmelcher, P. Entangling Lattice-Trapped Bosons with a Free Impurity: Impact on Stationary and Dynamical Properties. *Entropy* **2021**, *23*, 290. <https://doi.org/10.3390/e23030290>

Academic Editors: Ofir E. Alon and Axel U.J. Lode

Received: 5 February 2021
Accepted: 23 February 2021
Published: 26 February 2021

Publisher's Note: MDPI stays neutral with regard to jurisdictional claims in published maps and institutional affiliations.



Copyright: © 2021 by the authors. Licensee MDPI, Basel, Switzerland. This article is an open access article distributed under the terms and conditions of the Creative Commons Attribution (CC BY) license (<https://creativecommons.org/licenses/by/4.0/>).

1. Introduction

Multicomponent quantum gases can be experimentally studied with a high degree of controllability in the ultracold regime [1,2]. Specifically, two-component mixtures of bosons or fermions can be trapped in various species selective external geometries [3,4]. Few-body ensembles can be realized in particular in one-dimension (1D) [5,6] while the scattering lengths are tunable through Feshbach and confinement induced resonances [7,8]. In 1D bosonic mixtures the adjustability of the intercomponent interactions gives rise to intriguing phenomena such as phase-separation processes [9,10] in the repulsive regime, formation of bound states, e.g., droplet configurations [11,12] for attractive interactions as well as quasiparticle-like states in highly particle imbalanced systems [13,14].

In this latter context, an impurity species is embedded in an environment of the majority species called the medium. The presence of a finite impurity-medium coupling leads to an effective picture where the impurity properties deviate from the bare particle case exhibiting, for instance, an effective mass [15–18] and induced interactions [19–22] mediated by the medium. The resultant states are often called polarons [23,24] and have been experimentally realized mainly in higher-dimensions [25–29] and to a lesser extent in 1D [13,30] using spectroscopic schemes. Since these settings consist of a few-body subsystem they naturally show enhanced correlation properties, especially in 1D, rendering their many-body treatment inevitable. In particular, the emergent impurity-medium

entanglement can lead to spatial undulations of the medium. This mechanism is manifested, for instance, as sound-wave emission [17,31] and collective excitations [32,33] of the host or the formation of a bound state [34–36] between the impurity and atoms of the medium for attractive interspecies interactions.

Another relevant ingredient is the external trapping geometry that the two components experience. Indeed, for harmonically trapped and homogeneous systems remarkable dynamical features of impurity physics include the spontaneous generation of localized patterns [17,37–39], inelastic collisional aspects of driven impurities [40–42] with the surrounding and their relaxation at long timescales [43–45]. On the other hand, when a lattice potential is introduced the situation becomes more complicated giving rise, among others, to doped insulator physics [46,47] and impurity transport [48–50]. Apparently, configuring one component by manipulating its external trap while leaving the other intact, e.g., by using a species selective external potential, it is possible to control the response of the unperturbed component via the impurity-medium interaction [51,52]. For instance, operating in the lowest-band approximation it has been demonstrated that a lattice trapped impurity interacting with a homogeneous host exhibits besides tunneling dynamics [53] also self-trapping events [54,55] and can even undergo Bloch-oscillations [56]. The opposite case, where the medium resides in the lattice, provides an experimental probe of the impurity-medium collision parameters [57] and interaction strength [58].

In this work by considering an impurity in a box potential and a lattice trapped few-body medium we examine how the latter affects the impurity's spatial distribution by means of (de-)localization for different lattice depths and intercomponent interactions. Indeed, a lattice trapped medium can reside either in a superfluid or an insulating-like phase [46], a fact that is expected to crucially impact the impurity's configuration and vice versa [59]. To address the ground state properties and quantum quench dynamics of the above-discussed impurity setting we utilize the multi-layer multi-configuration time-dependent Hartree method for atomic mixtures (ML-MCTDHX) [60–62]. This variational method enables us to account for the relevant correlations of the mixture and operate beyond the lowest-band approximation for the medium.

Focusing on the ground state of the system and in order to testify its overall response for varying intercomponent interactions we determine the fidelity between the coupled and decoupled composite system both at the many-body and the single-particle level. Note that in impurity settings this observable is commonly termed residue [23,24] enabling us to identify, e.g., the polaron formation, while the influence of the impurity-medium entanglement in this observable is still an open issue. It is demonstrated that despite the fact that the total entangled state may strongly deviate from its decoupled configuration, this effect is arguably less pronounced or even diminished at the single-particle level. Furthermore, we showcase that the build-up of impurity-medium entanglement is sensitive to the interplay between the intercomponent interactions and the lattice depth [46]. Interestingly, stronger interactions do not necessarily lead to a larger amount of entanglement, whereas the state of the majority species may undergo substantial structural changes, which remain invisible at the single-particle level. Moreover, we identify the imprint of the background on the impurities and vice versa by relying on one- and two-body density distributions evincing a rich spatial structure of the components with respect to the lattice depth as well as the inter- and intracomponent interactions. In particular, it is argued that for repulsive (attractive) interactions the impurity delocalizes (localizes) around the central lattice site. The delocalization of the impurity is accompanied by its phase-separation with the majority component [63], where the impurity tends to the edges of the box for a superfluid background or exhibits a multi-hump structure for an insulating medium. We further analyze how much the intercomponent correlations are actually involved in the structural changes observed in the spatial probability distributions. To this end we compare density distributions of the numerically exact ground state to the corresponding ones of an approximate non-entangled ground state. We identify that the entanglement-induced

corrections accelerate phase-separation at repulsive couplings and generally slow down spatial localization at attractive interactions.

Finally, we monitor the non-equilibrium dynamics of the mixture. We prepare the system in a phase-separated, i.e., disentangled configuration, and quench the intercomponent interactions to smaller values resulting in the counterflow of the components and thus triggering their tunneling dynamics and the consequent build-up of entanglement. The majority component plays the role of a material barrier for the impurity [50,64] which performs tunneling oscillations whose period depends strongly on the impurity-medium interaction. The many-body nature of the tunneling process of the components is testified by invoking the individual natural orbitals constituting the time-evolved many-body state.

Our presentation is structured as follows. In Section 2, we introduce the impurity setting and in Section 3 we discuss our many-body treatment to tackle its ground state and dynamics. The ground state properties of the delocalized impurity and the lattice trapped medium are addressed in Section 4. We analyze the fidelity between perturbed and unperturbed (reduced) density operators, quantify the degree of entanglement and visualize its impact on single- and two-body density distributions of each species for different intra- and intercomponent interactions and lattice depths. The non-equilibrium dynamics of the mixture following a quench of the impurity-medium coupling to smaller values is discussed in Section 5. We provide a summary of our results and elaborate on future perspectives in Section 6.

2. Setup and Hamiltonian

We consider a single impurity particle immersed in a few-body system of ultracold bosons. Both components reside in a quasi-1D geometry ensured by a strong transversal confinement [13]. Along the longitudinal direction the N_A majority species atoms of mass m_A are trapped inside a lattice of depth V with l sites and length L with hard-wall boundary conditions. The impurity atom of mass m_B is subject to a box potential of the same length. The species-dependent trapping has been successfully demonstrated experimentally [3,4]. The inter-particle interactions are of s-wave contact type with g_{AA} denoting the majority-majority interaction strength and g_{AB} the majority-impurity coupling. Both may be tuned independently by a combination of Feshbach and confinement induced resonances [7,8]. Furthermore, we assume equal masses $m_A = m_B$, which corresponds to a mixture of the same isotope with the particles being distinguishable due to two different hyperfine states [65–70]. By introducing $R^* = L$ and $E^* = \hbar^2 / (mL^2)$ as length and energy scales we arrive at the following rescaled many-body Hamiltonian:

$$H = -\frac{1}{2} \frac{\partial^2}{\partial y^2} - \sum_i^{N_A} \left(\frac{1}{2} \frac{\partial^2}{\partial x_i^2} + V \sin^2(\pi l x_i) \right) + g_{AA} \sum_{i < j}^{N_A} \delta(x_i - x_j) + g_{AB} \sum_i^{N_A} \delta(x_i - y), \quad (1)$$

where y and x_i denote the spatial coordinates of the impurity and i th majority atom, respectively.

In this work we primarily focus on the ground state properties of the above many-body Hamiltonian Equation (1) with $l = 5$ lattice sites and $N_A = 5$ majority particles. In particular, we are interested in the susceptibility of the composite system to structural changes and the amount of inter-particle correlations it may hold. We cover a parameter space from moderately attractive to repulsive interaction strengths, i.e., $g_{AA} \in [-3.0, 3.0]E^*R^*$ and $g_{AB} \in [-5.0, 5.0]E^*R^*$, for a range of lattice depths from shallow to deep, namely $V \in [100, 1000]E^*$. In the following, we will refer to a lattice as being shallow ($V < 200$), moderately deep ($V \approx 500$) and very deep ($V > 800$). We remark that in recoil units the above parameters translate to $g_{AA} \in [-0.38, 0.38]E_{rec}x_{rec}$, $g_{AB} \in [-0.64, 0.64]E_{rec}x_{rec}$ and $V \in [0.81, 8.1]E_{rec}$. Additionally, we demonstrate how an initially disentangled state prepared in the immiscible regime acquires dynamically a finite amount of entanglement after quenching the intercomponent coupling g_{AB} , thus triggering a counter-flow tunneling process of the two components.

3. Variational Approach

In order to account for effects stemming from inter-particle correlations we rely on the Multi-Layer Multi-Configurational Time-Dependent Hartree Method for atomic mixtures (ML-MCTDHX), for short ML-X [60–62]. This ab-initio method has been successfully applied to solve the time-dependent Schrödinger equation of various experimentally accessible and extensively studied systems. The core idea of this method lies in expanding the many-body wave-function in terms of product states of time-dependent single-particle functions [71,72]. This becomes beneficial, when the number of basis configurations with considerable contribution to the state fluctuates weakly during the time propagation, whereas the configurations themselves do change. Taking a variationally optimal basis at each time-step allows us to cover the high-dimensional Hilbert space at a lower computational cost compared to a time-independent basis.

The wave function ansatz for a given system is decomposed in multiple layers. On the first layer, called top layer, we separate the degrees of freedom of the binary mixture into product states of majority and impurity species functions $|\Psi_i^\sigma(t)\rangle$ with $\sigma \in \{A, B\}$ and $i \in \{1, \dots, S\}$:

$$|\Psi(t)\rangle = \sum_{i=1}^S \sqrt{\lambda_i(t)} |\Psi_i^A(t)\rangle \otimes |\Psi_i^B(t)\rangle. \quad (2)$$

Here, the time-dependent coefficients $\lambda_i(t)$, normalized as $\sum_{i=1}^S \lambda_i(t) = 1$, determine the degree of entanglement between the components [73]. The choice of $S = 1$ results in the so-called species mean-field (SMF) approximation, meaning that no entanglement is assumed between the components [15]. In that case the intercomponent correlations, if present, are neglected and every component is effectively subject to an additional one-body potential induced by the fellow species [50,63]. In this work, we put a special emphasis on the impact of the entanglement on several one- and two-body quantities by comparing the numerically exact ground state to the corresponding SMF approximation.

On the second layer, called species layer, each species function $|\Psi_i^\sigma(t)\rangle$ is expanded in terms of species-dependent symmetrized product states of single-particle functions (SPFs) $|\varphi_j^\sigma(t)\rangle$ with $j \in \{1, \dots, s_\sigma\}$, accounting for the bosonic nature of our particles and abbreviated as $|\vec{n}^\sigma\rangle = |n_1^\sigma, \dots, n_{s_\sigma}^\sigma\rangle$:

$$|\Psi_i^\sigma(t)\rangle = \sum_{\vec{n}^\sigma | N_\sigma} C_{i, \vec{n}^\sigma}(t) |\vec{n}^\sigma(t)\rangle. \quad (3)$$

In this expression, the sum is performed over all configurations $\vec{n}^\sigma | N_\sigma$ obeying the particle-number constraint $\sum_{i=1}^{s_\sigma} n_i^\sigma = N_\sigma$. On the third and final layer, called primitive layer, each SPF is represented on a one-dimensional time-independent grid [74].

The Dirac-Frenkel variational principle [75] is subsequently applied to the above ansatz in order to derive the coupled equations of motion for the expansion coefficients $\lambda_i(t)$, $C_{i, \vec{n}^\sigma}(t)$ and the SPFs $|\varphi_j^\sigma(t)\rangle$. Finally, performing imaginary time-evolution one arrives at the ground state wave-function (4), whereas the real time-propagation allows to study the non-equilibrium dynamics of an arbitrary initial state (5). The results to be presented below have been obtained by using $(S, s_A, s_B) = (4, 5, 4)$ functions/SPFs on the top/species layers as well as 225 grid points on the primitive layer. We have carefully checked the convergence behavior of our results by comparing to simulations with a larger number of orbitals $(S, s_A, s_B) = (6, 8, 6)$ and found no significant changes for the quantities of interest.

In the following we will often refer to the reduced j -body density operators $\hat{\rho}_j^\sigma$ of species σ and the intercomponent reduced $(j+k)$ -body density operator $\hat{\rho}_{j+k}^{\sigma\bar{\sigma}}$ obtained from the many-body density operator $\hat{\rho} = |\Psi\rangle\langle\Psi|$:

$$\hat{\rho}_j^\sigma = \text{tr}_{N_\sigma \setminus j} \{ \text{tr}_{N_{\bar{\sigma}}} \{ \hat{\rho} \} \}, \quad (4)$$

$$\hat{\rho}_{j+k}^{\sigma\bar{\sigma}} = \text{tr}_{N_\sigma \setminus j} \{ \text{tr}_{N_{\bar{\sigma}} \setminus k} \{ \hat{\rho} \} \}, \quad (5)$$

where $N_\sigma \setminus j$ stands for integrating out $N_\sigma - j$ coordinates of component σ and $\bar{\sigma} \neq \sigma$. Of particular interest are the reduced one-body density operators $\hat{\rho}_1^A$ and $\hat{\rho}_1^B$ as well as the reduced two-body intra- and intercomponent density operators $\hat{\rho}_2^A$ and $\hat{\rho}_2^{AB}$, respectively, since they determine the expectation values of various experimentally accessible local one- and two-body observables, such as the average particle position, the inter-atomic distance or the wave-packet width.

4. Impact of Intercomponent Coupling on Ground State Properties

In Section 4.1, we analyze to which extent the many-body wave-function as well as the reduced one-body density operators are modified by the intercomponent interaction. To this end we analyze the fidelity between the interacting and non-interacting (reduced) density operators, which is a measure of their closeness. We find that with increasing absolute value of the interaction strength the system is more robust w.r.t. changes on the one-body as compared to the many-body level. Moreover, each component is affected differently depending on the lattice depth and majority interaction strength.

Subsequently, in Section 4.2 we quantify the degree of entanglement by means of the von Neumann entropy and identify parameter regions with substantial inter-particle correlations. Interestingly, increasing the absolute value of the intercomponent coupling does not always result in stronger entanglement. In fact, there are parameter regions where a strongly interacting ground state becomes almost orthogonal to the non-interacting one and the components remain to a good approximation disentangled.

Finally, we combine insights from Sections 4.1 and 4.2 to identify interesting parameter regimes and perform an in-depth analysis of the underlying physical phenomena in Section 4.3. In particular, we inspect how the spatial representation of density operators is altered and compare those to the corresponding SMF results. The latter allows us to spatially resolve the corrections to the SMF densities induced by the entanglement and interpret its impact as acceleration or deceleration of the undergoing processes, e.g., the phase separation or localization.

4.1. Fidelity for Quantifying the Impact of the Intercomponent Interaction

First, we aim to analyze how the intercomponent coupling g_{AB} impacts the ground state of non-interacting species (NIS) at $g_{AB} = 0$. For this purpose, we evaluate the fidelity [76] of two density operators $\hat{\rho}$ and $\hat{\sigma}$ defined as:

$$F(\hat{\rho}, \hat{\sigma}) = \left(\text{tr} \sqrt{\sqrt{\hat{\rho}} \hat{\sigma} \sqrt{\hat{\rho}}} \right)^2 = F(\hat{\sigma}, \hat{\rho}). \quad (6)$$

We start with the fidelity between a NIS many-body density $\hat{\rho}_0 = |\Psi_0\rangle \langle \Psi_0|$ and a many-body density $\hat{\rho}_g = |\Psi_g\rangle \langle \Psi_g|$ for some finite coupling g_{AB} (Figure 1). Since both density operators describe pure states, Equation (6) reduces to $F_{mb} = |\langle \Psi_0 | \Psi_g \rangle|^2$. This measure, F_{mb} , is also known as the polaron residue studied in the context of phonon dressing of an impurity particle immersed in a bath of majority atoms [23,24].

For a weakly interacting ($g_{AA} = 0.5$) majority component Figure 1a we observe that the many-body fidelity at a fixed lattice depth decreases monotonously with the modulus of the coupling strength g_{AB} . At deep lattices the rate of its reduction is larger, a behavior which is even more pronounced at strong negative g_{AB} , where the interacting state becomes almost orthogonal to the non-interacting one ($g_{AB} = -5$ and $V = 1000$). The black dashed line encircles a parameter region of instability where the SMF ansatz collapses to a configuration with broken parity symmetry. For a moderately interacting ($g_{AA} = 3.0$) majority component Figure 1b the many-body fidelity becomes much more stable. Contrarily to Figure 1a the rate of reduction with g_{AB} is larger at shallow lattices instead. Finally, for a moderately deep ($V = 500$) lattice Figure 1c we observe a peculiar fast decay around $g_{AA} \approx -1$ starting at $g_{AB} < -2$. Additionally, at $g_{AA} \approx -1$ and positive g_{AB} there is a small pronounced decay region (black dashed circle), which is absent in the SMF approximation.

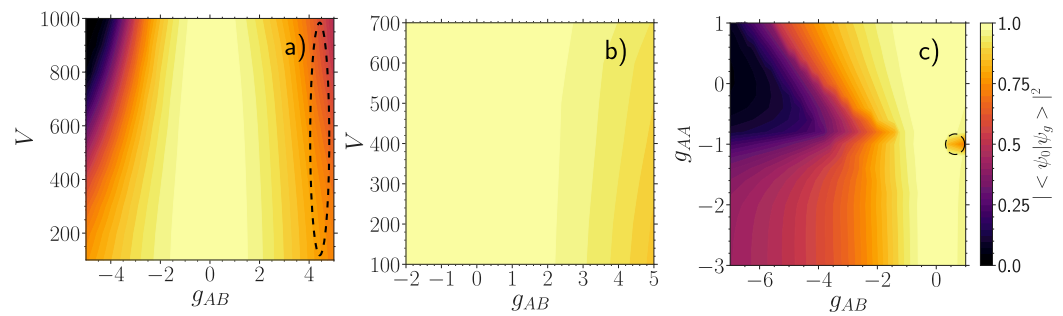


Figure 1. Fidelity $|\langle \Psi_0 | \Psi_g \rangle|^2$ between a many-body state $|\Psi_0\rangle$ at $g_{AB} = 0$ and a many-body one $|\Psi_g\rangle$ at finite g_{AB} , for (a) $g_{AA} = 0.5$, (b) $g_{AA} = 3.0$ and (c) $V = 500$ as a function of the majority-impurity coupling g_{AB} and the lattice depth V (a,b) or the interaction strength of the majority atoms g_{AA} (c). All quantities are given in box units with characteristic length $R^* = L$ and energy $E^* = \hbar^2 / (mL^2)$ with L denoting the extension of the box trap. Regions encircled by black dashed lines indicate parameter regions with substantial qualitative differences to the SMF ansatz.

Next, we analyze the fidelity between a free impurity described by a pure state $|\Phi_0\rangle \langle \Phi_0|$ and an entangled one $\hat{\rho}_1^B$, in general being a mixed state Figure 2. Equation (6) then simplifies to $F_1^B = |\langle \Phi_0 | \hat{\rho}_1^B | \Phi_0 \rangle|^2$. This measure allows to judge to which extent the impurity atom is still a "free" particle of mass m_B . We emphasize that it should not be confused with a polaron quasi-particle having a renormalized effective mass. We observe that F_1^B follows overall a similar pattern as the many-body fidelity F_{mb} , but with a significantly slower decay rate. Though there are some strong qualitative differences, see in particular Figure 2c. Namely, the abrupt decay of F_{mb} around $g_{AA} \approx -1$ at negative g_{AB} Figure 1c is absent in F_1^B along with the small decay region at positive g_{AB} (black dashed circle). From this we anticipate that the majority component is responsible for these features in F_{mb} .

For the above reason, we now investigate the complementary fidelity $F_1^A = F(\hat{\rho}_1^A(g_{AB} = 0), \hat{\rho}_1^A)$, i.e., between mixed states characterizing a majority particle in the NIS state $\hat{\rho}_1^A(g_{AB} = 0)$ and in the interacting state $\hat{\rho}_1^A$ Figure 3. This quantity captures to which extent a majority particle is still in a mixed state induced solely by the intraspecies interaction strength g_{AA} . In case of a weak g_{AA} Figure 3a F_1^A is notably affected only at deep lattices $V > 600$ and strong negative coupling $g_{AB} < -4$. For large g_{AA} Figure 3b we observe that the intercomponent correlations are not strong enough to overcome the intraspecies ones, thus barely affecting the mixedness of the NIS majority state, since $F_1^A \approx 1$ in the whole range $-2 < g_{AB} < 5$ and $100 < V < 700$. In Figure 3c we find evidence that the majority component is indeed responsible for the particular decay patterns observed in the many-body fidelity F_{mb} , which were absent in F_1^B . Overall, the majority component demonstrates a higher level of robustness at the single-particle level as compared to the impurity.

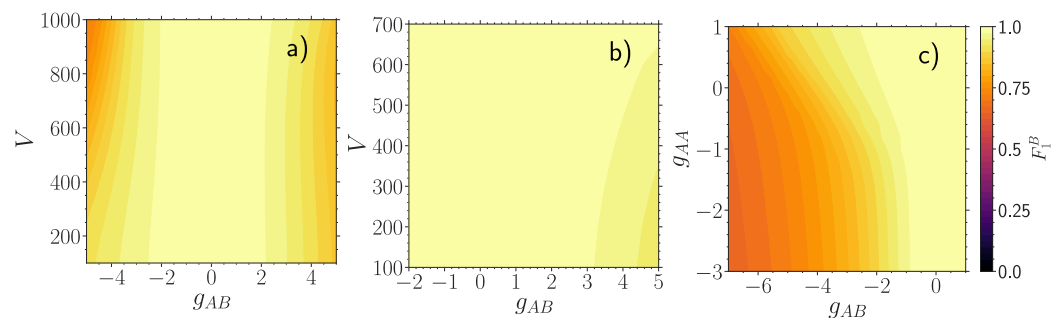


Figure 2. Fidelity $F_1^B = |\langle \Phi_0 | \hat{\rho}_1^B | \Phi_0 \rangle|^2$ between a free impurity particle $|\Phi_0\rangle$ at $g_{AB} = 0$ and an entangled one $\hat{\rho}_1^B$ at finite g_{AB} , for (a) $g_{AA} = 0.5$, (b) $g_{AA} = 3.0$ and (c) $V = 500$ and varying majority-impurity coupling g_{AB} and the lattice depth V or the interaction strength of the majority atoms g_{AA} . All quantities are expressed in box units with characteristic length $R^* = L$ and energy $E^* = \hbar^2 / (mL^2)$ while L is the extension of the box trap.

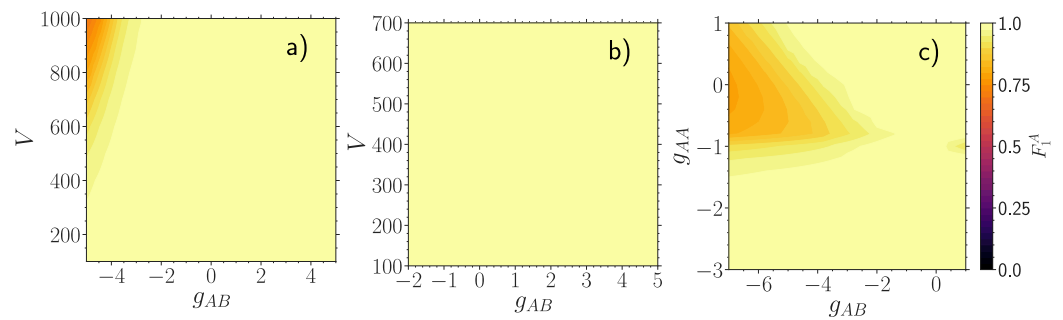


Figure 3. Fidelity $F_1^A = F(\hat{\rho}_1^A, \hat{\rho}_1^A(g_{AB} = 0))$ between mixed states characterizing a majority particle when the medium is disentangled $\hat{\rho}_1^A(g_{AB} = 0)$ and entangled $\hat{\rho}_1^A$ with the impurity atom, for (a) $g_{AA} = 0.5$, (b) $g_{AA} = 3.0$ and (c) $V = 500$ as a function of the majority-impurity coupling g_{AB} and the lattice depth V (a,b) or the interaction strength of the majority atoms g_{AA} (c). All quantities are provided in box units of characteristic length $R^* = L$ and energy $E^* = \hbar^2/(mL^2)$ with L being the extension of the box trap.

4.2. Entropy Measures for Quantifying the Degree of Correlations

As we have seen in the previous section, an initially disentangled composite system may be drastically influenced by the intercomponent coupling. However, it is far from obvious to which extent the correlations are actually involved when the ground state undergoes structural changes [77]. For instance, a strongly interacting ground state may in fact just represent a different disentangled state or a state seemingly unaffected by the coupling may feature substantial correlations which guarantee its robustness. To investigate these intriguing possibilities we perform a further classification based on the degree of inter-particle correlations.

To quantify the degree of correlations in our impurity system we use the von Neumann entropy of the reduced density operators [78]. Here, we distinguish between the entanglement entropy S_{vN} of the reduced density operator $\hat{\rho}^\sigma$ of species σ [9,46] and the fragmentation entropy S_{vN}^σ of the reduced one-body density operator $\hat{\rho}_1^\sigma$ of species σ [52,79,80]. The former, $\hat{\rho}^\sigma$, is obtained by tracing the density operator $\hat{\rho}$ of the composite many-body system over one of the species, while the latter, $\hat{\rho}_1^\sigma$, by additionally tracing $\hat{\rho}^\sigma$ over all of the particles of the remaining component except one. In the presence of correlations the resulting reduced density operator will describe a mixed state. The entanglement entropy is caused by intercomponent correlations whereas the fragmentation entropy is primarily a signature of intracomponent ones, though it can be greatly impacted once the intercomponent correlations become dominant. Explicitly, the entanglement and fragmentation entropies are given as:

$$S_{vN} = -\text{tr}(\hat{\rho}^\sigma \ln \hat{\rho}^\sigma) = -\sum_{i=1}^S \lambda_i \ln \lambda_i \quad \text{with } \hat{\rho}^\sigma = \text{tr}_{\bar{\sigma}}(\hat{\rho}) = \sum_{i=1}^S \lambda_i |\Psi_i^\sigma\rangle \langle \Psi_i^\sigma|, \quad (7)$$

$$S_{vN}^\sigma = -\text{tr}(\hat{\rho}_1^\sigma \ln \hat{\rho}_1^\sigma) = -\sum_{i=1}^{s_\sigma} n_i^\sigma \ln n_i^\sigma \quad \text{with } \hat{\rho}_1^\sigma = \text{tr}_{N_\sigma-1}(\hat{\rho}^\sigma) = \sum_{i=1}^{s_\sigma} n_i^\sigma |\Phi_i^\sigma\rangle \langle \Phi_i^\sigma|. \quad (8)$$

In these expressions, λ_i and $|\Psi_i^\sigma\rangle$ denote the natural populations and natural orbitals of the spectrally decomposed $\hat{\rho}^\sigma$, while n_i^σ and $|\Phi_i^\sigma\rangle$ are the natural populations and natural orbitals of the spectrally decomposed $\hat{\rho}_1^\sigma$ [60,72]. Furthermore, S and s_σ are the number of species orbitals and single-particle functions, respectively, N_σ is the number of σ component particles and $\sigma \neq \bar{\sigma}$.

In the following, we display the species entanglement S_{vN} from Equation (7) Figure 4 and the majority fragmentation S_{vN}^A from Equation (8) Figure 5 as a function of the majority-impurity coupling g_{AB} and the lattice depth V or the interaction strength of the majority atoms g_{AA} . In case the entanglement entropy S_{vN} is close to zero, the

corresponding subsystems are to a very good approximation disentangled. Thus, making a SMF ansatz in Equation (2) would greatly facilitate numerical calculations while providing quantitatively good results for physical observables. On the other hand, already moderate values of entanglement may have an impact on some physical quantities with measurable differences to the SMF approximation, whereas local peaks may indicate phase transitions [10,81,82]. Regarding the fragmentation entropy of interacting majority atoms S_{vN}^A it is highly non-trivial to predict how their intrinsic mixedness, caused by the intra-particle interactions g_{AA} , can be changed by the intercomponent coupling g_{AB} .

4.2.1. Weakly Repulsive Interacting Majority Component

For a weakly interacting majority component with $g_{AA} = 0.5$, the entanglement entropy S_{vN} Figure 4a displays two different behaviors depending on the sign of the coupling strength. For positive g_{AB} it increases gradually with increasing coupling strength g_{AB} , with the build-up being faster for a deeper lattice [52]. This is related to the onset of phase separation taking place sooner for a deeper lattice with increasing g_{AB} (see also the discussion in Section 4.3). Turning to negative g_{AB} the entanglement entropy first grows gradually with decreasing coupling strength g_{AB} , but then, for larger V below some threshold value, the entanglement reduces to almost zero ($g_{AB} < -4$ and $V > 600$). Apart from the above mentioned pattern the overall behavior of S_{vN} in Figure 4a is very similar to the one observed in the corresponding many-body fidelity Figure 1a.

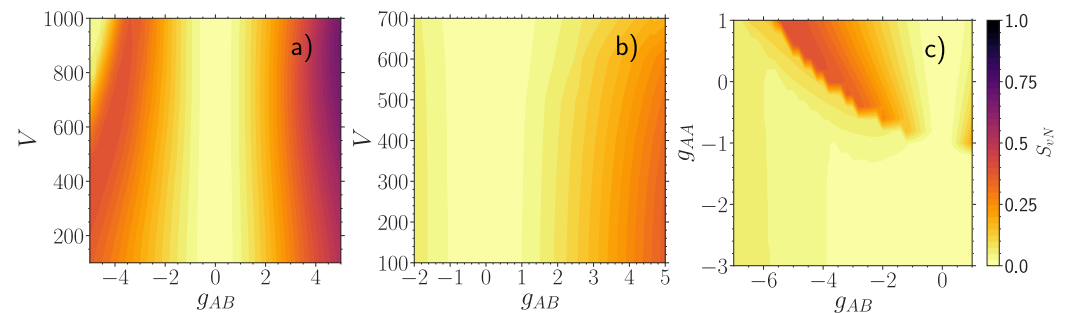


Figure 4. Entanglement entropy S_{vN} , see Equation (7), for (a) $g_{AA} = 0.5$, (b) $g_{AA} = 3.0$ and (c) $V = 500$ with varying majority-impurity coupling g_{AB} and the lattice depth V (a,b) or the interaction strength of the majority atoms g_{AA} (c). All quantities are given in box units with characteristic length $R^* = L$ and energy $E^* = \hbar^2/(mL^2)$ with L denoting the extension of the box trap.

The fragmentation entropy of the majority component S_{vN}^A Figure 5a at $g_{AB} = 0$ is larger for a deeper lattice. The reason is that the ratio of the intraspecies interaction energy and the single-particle energy of the majority component increases with a larger V or g_{AA} . In the limit of an infinitely deep lattice or an infinitely strong intraspecies repulsion we expect full fermionization, meaning that the one-body density operator becomes a mixed state with a uniform distribution of natural orbitals and the fragmentation entropy of the majority component reaches the value $\ln(N_A) \approx 1.6$. However, we observe that we are operating far away from that limit, since $\max S_{vN}^A < 0.4$.

At positive g_{AB} , as the entanglement entropy S_{vN} builds up Figure 4a, the fragmentation entropy S_{vN}^A of the majority component at $g_{AB} = 0$ is more robust to variations of g_{AB} at deeper lattice depths compared to shallow lattices Figure 5a. Once the entanglement becomes strong enough to overcome intracomponent correlations, the fragmentation entropy of the majority atoms starts to increase with a fast rate (e.g., $V = 1000$, $g_{AB} > 4$). At negative g_{AB} , if the medium features a small fragmentation entropy at $g_{AB} = 0$ ($V < 900$), then S_{vN}^A rises first with decreasing g_{AB} , reaches a local maximum and finally drops to very small values at a sufficiently strong coupling strength. In contrast, if the fragmentation entropy of the decoupled majority component has already reached a moderate magnitude ($V > 900$), then the initial fragmentation is gradually reduced with decreasing g_{AB} , until finally both entropies become negligibly small ($g_{AB} < -4$). Once that happens, the resulting

many-body state becomes to a good approximation a disentangled composite state with a condensed majority component.

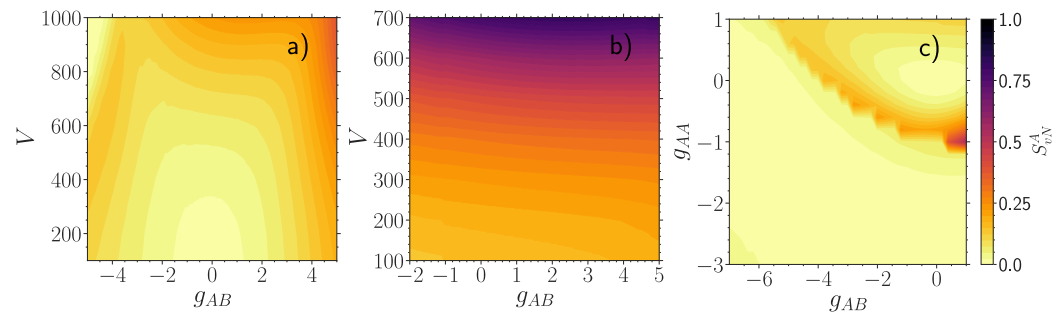


Figure 5. Fragmentation entropy S_{vN}^A , see Equation (8), for (a) $g_{AA} = 0.5$, (b) $g_{AA} = 3.0$ and (c) $V = 500$ with respect to the majority-impurity coupling g_{AB} and the lattice depth V (a,b) or the interaction strength of the majority atoms g_{AA} (c). All quantities are provided in terms of box units with characteristic length $R^* = L$ and energy $E^* = \hbar^2/(mL^2)$ while L denotes the extension of the box trap.

4.2.2. Moderately Repulsive Interacting Majority Component

The entanglement entropy S_{vN} of a moderately interacting majority medium at $g_{AA} = 3.0$ in Figure 4b displays the same qualitative behavior as the many-body fidelity F_{mb} shown in Figure 1b. Contrary to $g_{AA} = 0.5$ the entanglement is overall less pronounced and builds up faster at shallow lattice depths instead. Such a comparatively weak entanglement leaves only a minor imprint on the fragmentation of the majority component S_{vN}^A , see Figure 5b, manifested as a weak dependence on the coupling g_{AB} . The fragmentation of the majority species is substantial compared to $g_{AA} = 0.5$ Figure 5a at the same lattice depth. Nevertheless, the fermionization limit is not yet reached, since $\max S_{vN}^A \approx 0.8$. The intercomponent correlations are not strong enough to overcome the intraspecies ones in accordance with the robustness of the majority component observed on the one-body level in Figure 3b. From this we expect a rather small impact of entanglement on observables, which depend solely on the majority particle distribution.

4.2.3. Attractively Interacting Majority Component

Finally, we analyze the dependence of the above-described entropy measures on the intraspecies interaction strength g_{AA} for a moderately deep lattice depth $V = 500$ Figures 4c and 5c. Since repulsive interactions have been already amply covered, we here concentrate on negative g_{AA} and g_{AB} .

As it can be readily seen, there is a parameter sector at $g_{AB} < 0$ and $g_{AA} > -1$ containing high values for the entanglement entropy S_{vN} Figure 4c. This sector displays a similar behavior to S_{vN} in Figure 4a at negative couplings, namely starting from the decoupled regime, the entanglement grows with decreasing g_{AB} , only to drastically decrease below some negative threshold value of g_{AB} . This threshold for g_{AB} lies at lower values the higher the intracomponent interaction strength g_{AA} is. We find that this abrupt decay of S_{vN} coincides with the one observed in the many-body fidelity F_{mb} Figure 1c. This suggests that the disappearance of intercomponent correlations leads to an increased susceptibility of the system to g_{AB} variation. The other decay region, present in F_{mb} at $g_{AA} \approx -1$ and negative g_{AB} , is missing in the entanglement entropy S_{vN} . From this we infer that it can be understood within the SMF picture. Additionally, there is also another much smaller sector characterized by a high entanglement entropy at $g_{AB} > 0$ and $g_{AA} \approx -1$. It is directly related to structural changes observed in F_{mb} and F_1^A at the same values Figures 1c and 3c, which would have been absent in the SMF picture. Apart from that, below $g_{AA} < -1$ the entanglement entropy among the components is either absent or of minor relevance.

Previously, we have mentioned that an isolated majority species, which interacts repulsively ($g_{AA} > 0$), features a higher degree of fragmentation the larger g_{AA} is. In

the case of attractive interactions ($g_{AA} < 0$), however, the situation is different. Namely, starting from $g_{AA} = 0$ the fragmentation entropy tends first to increase with decreasing g_{AA} , but then decreases up to the point of describing approximately a condensed state again see Figure 5c at $g_{AB} = 0$. Regarding the impact of the intercomponent coupling g_{AB} on S_{vN}^A we observe overall very similar patterns as for the entanglement entropy S_{vN} Figure 4c. Regions where both entropic measures S_{vN} and S_{vN}^A are of small magnitude remind of the corresponding sectors in Figures 4a and 5a at $V > 800$ and $g_{AB} < -4$.

4.3. Single- and Two-Particle Density Distributions

The measures of fidelity and entropy discussed in the previous sections are very useful in identifying parameter regions being substantially impacted and/or highly correlated indicating regimes of high interest for further investigation. However, they do not provide insights into the actually undergoing processes. To get a better understanding we ask for the impact on measurable quantities such as the one-body and two-body density distribution functions, which can be accessed by fluorescence imaging with a quantum gas microscope [83–87].

In the following, $\rho_1^\sigma(z)$ describes the probability density to find a single particle of species σ at position z , while $\rho_2^{\sigma\bar{\sigma}}(z_1, z_2)$ denotes the probability density to simultaneously measure one particle of species σ at position z_1 and another one of the same or different species $\bar{\sigma}$ at position z_2 . The expectation value of any local observable depending on up to two degrees of freedom can be evaluated as an overlap integral with the appropriate probability density. Since many local observables often depend only on the distance between the particles, i.e., $O(z_1, z_2) = O(z_1 - z_2)$, we replace $\rho_2^{\sigma\bar{\sigma}}(z_1, z_2)$ by the probability density $\rho_r^{\sigma\bar{\sigma}}(r)$ to measure two particles belonging to the same or different species at a relative distance r independent of their individual positions. To this end we perform a coordinate transformation $R = (z_1 + z_2)/2$ and $r = z_1 - z_2$ giving the following identity:

$$\int \rho_2^{\sigma\bar{\sigma}}(z_1, z_2) dz_1 dz_2 = \int \rho_r^{\sigma\bar{\sigma}}(r, R) dr dR. \quad (9)$$

Then we define:

$$\rho_r^{\sigma\bar{\sigma}}(r) = \int \rho_2^{\sigma\bar{\sigma}}(r, R) dR. \quad (10)$$

Our first goal here is to investigate how the above mentioned quantities are affected in parameter sectors displaying strong susceptibility to structural changes identified in Section 4.1 and, in particular, whether the density distributions are capable to capture the undergoing changes in the many-body state.

Our second goal is to extract the impact of the entanglement. To this end we compare the above density distributions obtained from the variational ML-X calculations to the ones where the SMF ansatz is assumed. The latter will be distinguished by a tilde sign placed on top of the corresponding quantities. In the following, we shall evince that a large entanglement entropy identified in Section 4.2 has indeed a notable impact, but not always on all of the above mentioned density distributions. Thus, it may enhance or impede the effects coming from the induced SMF potential, such as phase separation and localization, or affect the bunching properties of the majority component.

4.3.1. Weakly Repulsive Interacting Majority Component

For a shallow lattice ($V = 100$) we observe in Figure 6 that the majority component (panel a1) at $g_{AB} = 0$ occupies mainly the central site (at $z = 0$) and the two intermediate ones (at $z = \pm 0.2$), while ρ_r^{AA} (panel c1) features an almost Gaussian shape due to weak intraspecies correlations. At moderate positive couplings ($g_{AB} > 3$) both quantities are only slightly affected in accordance with the robustness of F_1^A in this interaction regime Figure 3a. At moderate negative couplings ($g_{AB} < -3$) both ρ_1^A and ρ_r^{AA} shrink with decreasing g_{AB} indicating an increased bunching tendency of the majority atoms towards the central lattice

site. The impact of entanglement here is moderate. It leads to an increased probability for the majority component to occupy the two intermediate sites, while disfavoring the central site (panel a2). Thus, it acts as an inhibitor of localization at negative g_{AB} and counteracts changes induced by the SMF potential at positive g_{AB} . Furthermore, entanglement favors bunching of the majority particles independent of the sign of the coupling (panel c2).

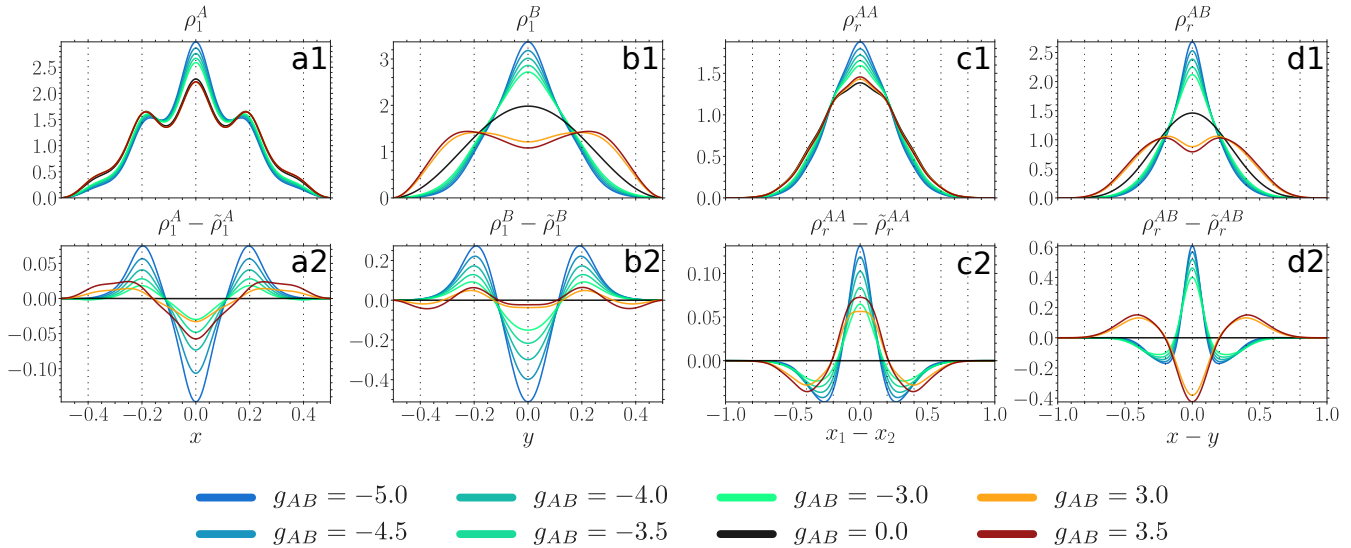


Figure 6. Upper panels: one-body probability densities $\rho_1^A(x)$, $\rho_1^B(y)$ (see Equation (4)) and distance probability distributions $\rho_r^{AA}(x_1 - x_2)$, $\rho_r^{AB}(x - y)$ (see Equation (10)) at $g_{AA} = 0.5$, $V = 100$ and for various values of g_{AB} (see legend). Lower panels: difference between probability densities obtained from the variational ML-X simulations and the SMF ansatz, the latter distinguished by a tilde sign. All quantities are given in box units with characteristic length $R^* = L$ and energy $E^* = \hbar^2 / (mL^2)$ with L being the extension of the box trap.

The decoupled impurity particle (panel b1) occupies the ground state of the box potential. At moderate positive couplings it develops two humps and forms a shell around the majority component density, a signature of phase separation [46,63] further confirmed by the appearance of two humps in ρ_r^{AB} (panel d1). At negative couplings ρ_1^B and ρ_r^{AB} shrink with decreasing g_{AB} accumulating around the trap center. The entanglement favors the process of phase separation at positive couplings and bunching between the two species at negative couplings (panel d2), while slowing down the shrinking of ρ_1^B at negative coupling (panel b2). We also remark that upon reaching a certain threshold value of $g_{AB} > 4$, the SMF solution experiences breaking of parity symmetry, causing substantial differences to the many-body symmetry-preserving solution (not shown).

For a deep lattice ($V = 1000$) in Figure 7 the majority component (panel a1) at $g_{AB} = 0$ displays an almost uniform distribution over all the lattice sites, while ρ_r^{AA} (panel c1) features a multi-hump structure due to stronger intraspecies correlations cf. Figure 5a). At moderate positive couplings ($g_{AB} > 3$) the width of ρ_1^A and ρ_r^{AA} is only slightly increased, again in accordance with the robustness of F_1^A Figure 3a). Thus, the majority component, experiencing the presence of a repelling impurity atom, shows a slight enhancement of the already present delocalization over the lattice. At moderate negative couplings ($g_{AB} < -3$) both ρ_1^A and ρ_r^{AA} shrink with decreasing g_{AB} to the extent where all atoms occupy predominantly only the central site ($g_{AB} < -4$). Such a large difference to the non-interacting ground state is in accordance with the observations made in F_1^A Figure 3a).

The impact of entanglement is structurally different compared to a shallow lattice (panels a2 and c2). At positive couplings, the entanglement greatly increases the probability for the majority atoms to be found at the central site, while decreasing the probability at outer sites ($z = \pm 0.4$) and being indifferent to the intermediate sites (panel a2). Additionally, it favors the bunching of the majority particles at the same or neighboring sites and

disfavors them being more than two sites apart (panel c2). At negative couplings, it acts in a similar way as in the case of shallow lattices, except that for a sufficiently strong coupling strength ($g_{AB} < -4$), where both entropy measures are of small magnitude see Figures 4a and 5a, the SMF ansatz is in good accordance with the many-body solution.

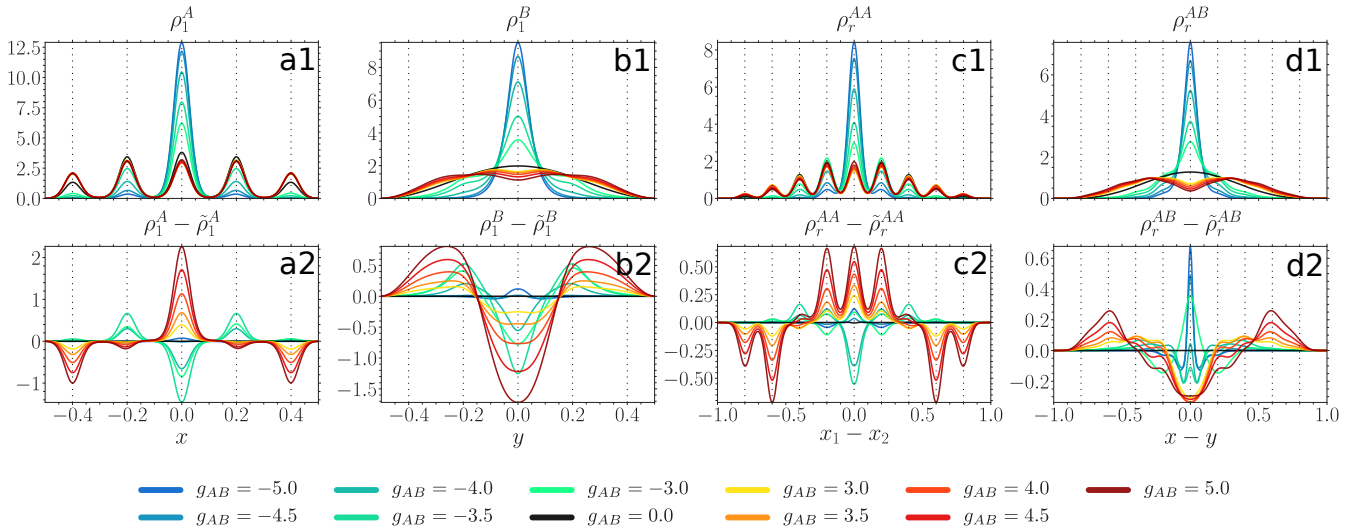


Figure 7. Upper panels: one-body probability densities $\rho_1^A(x)$, $\rho_1^B(y)$ (see Equation (4)) and distance probability distributions $\rho_r^{AA}(x_1 - x_2)$, $\rho_r^{AB}(x - y)$ (see Equation (10)) at $g_{AA} = 0.5$, $V = 1000$ and for various values of g_{AB} (see legend). Lower panels: difference between probability densities obtained from many-body ML-X calculations and SMF ansatz, the latter distinguished by a tilde sign. All quantities are given in box units with characteristic length $R^* = L$ and energy $E^* = \hbar^2/(mL^2)$ with L denoting the extension of the box trap.

The impurity particle (panel b1) at positive couplings ($g_{AB} > 3$) first develops two humps, but then as the coupling increases, the relative distance between those peaks grows, while the humps themselves become flatter. There is a strong signature of an onset of a four-peak structure at $g_{AB} = 5$. This is in accordance with the increasing relative distance between the species (panel d1) and the fact that the majority atoms are distributed uniformly over all the lattice sites in contrast to $g_{AA} = 0.5$, where the majority component was occupying mainly the central and the intermediate sites. At negative couplings ($g_{AB} < -3$) ρ_1^B and ρ_r^{AB} shrink with decreasing g_{AB} .

The entanglement favors the process where the impurity atom moves from the box center to its boundaries independently of the sign of the coupling (panel b2). At $g_{AB} < -4.0$ it plays only a minor role, the same as for the majority component. Regarding ρ_r^{AB} , at positive couplings the entanglement favors the process of phase separation by pushing the impurity particle more than two sites apart from a majority atom (panel d2). At negative couplings it enhances the bunching between the two species, even when the entanglement entropy is very small (e.g., at $g_{AB} = -5.0$).

4.3.2. Moderately Repulsive Interacting Majority Component

Considering our findings regarding fidelity and entropy measures we investigate here only shallow lattices at positive couplings Figure 8, where the structural changes caused by the coupling and the entanglement entropy S_{vN} may have a sizable impact on density distributions. The decoupled density of the majority component (panel a1) has three pronounced humps at the central ($z = 0$) and intermediate sites ($z = \pm 0.2$). The profile is overall more spread compared to a weakly interacting majority (cf. Figure 6 panel a1). Indeed, it is most beneficial for two particles to occupy neighboring sites (see the two humps in panel c1). The majority component gets only a weak feedback from the presence of a repulsive impurity atom, even at coupling strengths comparable to g_{AA} in accordance with the robustness of F_1^A in Figure 3b. The role of the entanglement is also

rather weak, though qualitatively different to $g_{AA} = 0.5$ in Figure 6. Thus, it increases the probability for the majority particle to be found at the region enclosed between the two intermediate sites, while decreasing the probability to be detected outside of that region (panel a2). Furthermore, it favors particle distances of a half lattice constant ($a_l = 0.2R^*$) (panel c2).

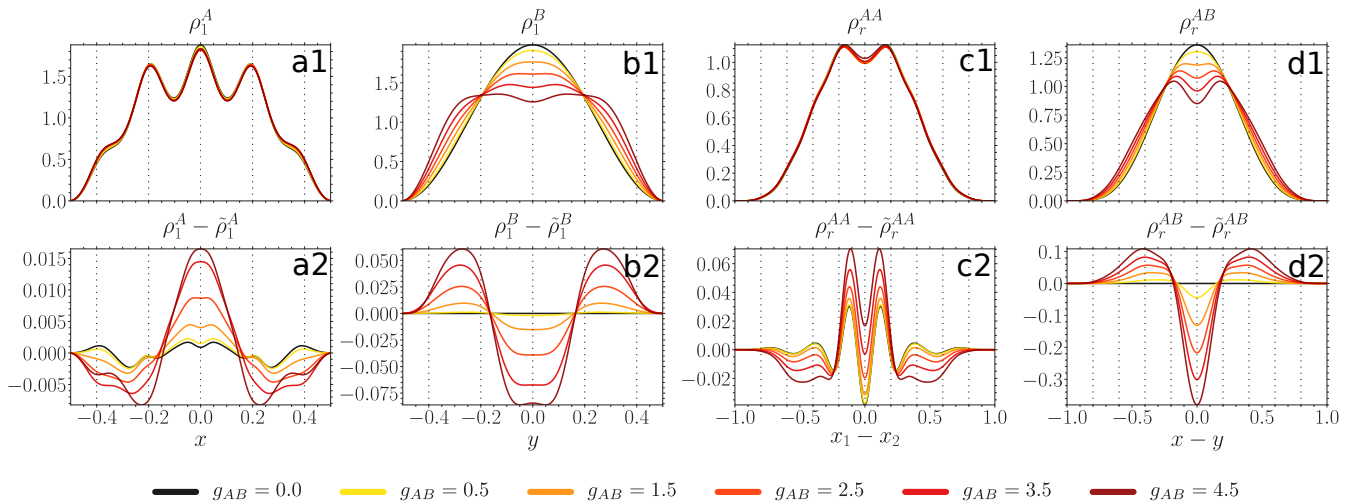


Figure 8. Upper panels: one-body probability densities $\rho_1^A(x)$, $\rho_1^B(y)$ (see Equation (4)) and distance probability distributions $\rho_r^{AA}(x_1 - x_2)$, $\rho_r^{AB}(x - y)$ (see Equation (10)) at $g_{AA} = 3.0$, $V = 100$ and for different values of g_{AB} (see legend). Lower panels: difference between probability densities obtained from the many-body ML-X calculations and SMF ansatz, the latter distinguished by a tilde sign. All quantities are provide in terms of box units with characteristic length $R^* = L$ and energy $E^* = \hbar^2 / (mL^2)$ while L is the extension of the box trap.

The impurity particle (panel b1) experiences phase separation similar to Figure 6 (panel b1), i.e., upon increasing g_{AB} it develops two humps with a minimum at the trap center. Then, those humps separate and flatten, until finally they would form a four-hump structure with three local minima located at the position of the three peaks in the majority component density (compare to panel a1). The separation between the species is again clearly manifested as two humps in ρ_r^{AB} with favored distance of a lattice constant ($a_l = 0.2R^*$) (panel d1). The entanglement affects the impurity atom in quite an opposite way when compared to the majority component (panel b2), i.e., it decreases the probability for the impurity atom to be found at the region enclosed between the two intermediate sites, while increasing the probability to lie outside of that region. Additionally, similar to the behavior at weaker g_{AA} (cf. Figure 6 panel d2), the entanglement accelerates the phase separation process (panel d2).

4.3.3. Attractively Interacting Majority Component

Finally, we concentrate on negative intraspecies interactions g_{AA} , namely a weak negative $g_{AA} = -0.4$ at negative g_{AB} Figure 9, contained in the parameter sector with substantial entanglement entropy Figure 4c.

In Figure 9, a decoupled majority atom where $g_{AB} = 0$ is localized at the central ($z = 0$) and intermediate ($z = \pm 0.2$) wells (panel a1). Even though the majority atoms are attracted to each other, the probability to be one or even two wells apart is still sizable (panel c1). With decreasing g_{AB} both ρ_1^A and ρ_r^{AA} shrink to a Gaussian. The impact of entanglement is quite different compared to the previously considered cases. Thus, at $g_{AB} > -4.8$ the entanglement slows down the process of ρ_1^A localization at the central well (panel a2). The strongest impact is reached around $g_{AB} \approx -2.4$, where the entanglement entropy is largest for the given value of intracomponent interaction $g_{AA} = -0.4$ Figure 4c. Below $g_{AB} < -4.8$, as the entanglement entropy suddenly drops, so does the difference to the SMF ansatz. The intercomponent correlations favor clustering of the majority atoms at

$-2.4 < g_{AB} < 0$ and $g_{AB} < -4.2$, whereas at $-4.2 < g_{AB} < -2.4$, where the entanglement entropy is largest, they inhibit the clustering (panel c2).

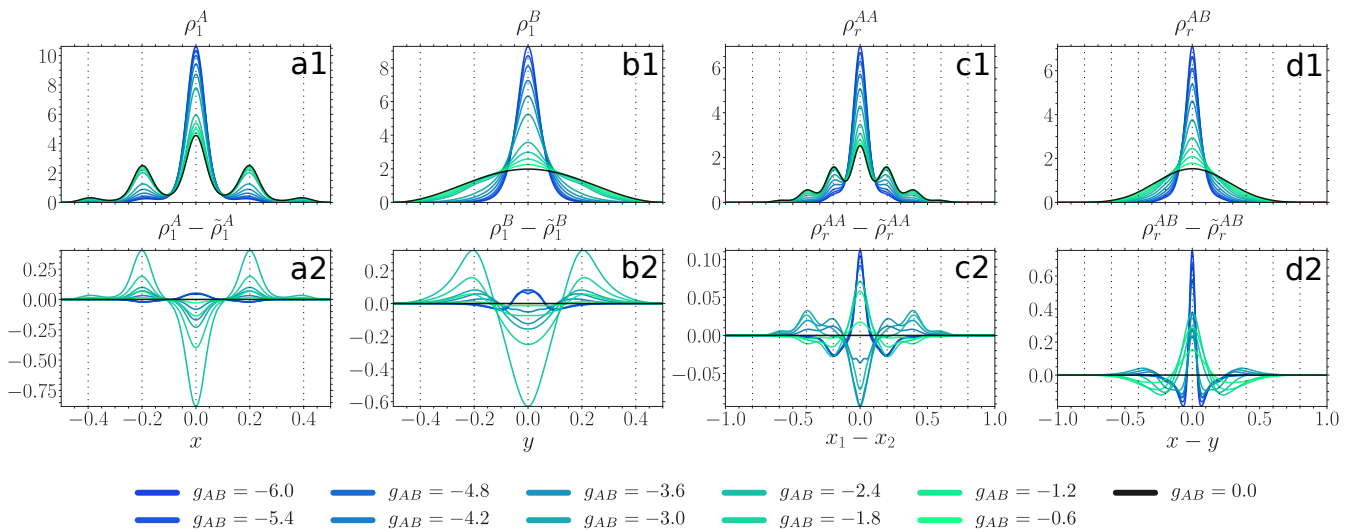


Figure 9. Upper panels: one-body probability densities $\rho_1^A(x)$, $\rho_1^B(y)$ (see Equation (4)) and distance probability distributions $\rho_r^{AA}(x_1 - x_2)$, $\rho_r^{AB}(x - y)$ (see Equation (10)) at $g_{AA} = -0.4$, $V = 500$ and for various values of g_{AB} (see legend). Lower panels: difference between probability densities obtained from the variational ML-X simulations and SMF ansatz, the latter distinguished by a tilde sign. All quantities are expressed in box units of characteristic length $R^* = L$ and energy $E^* = \hbar^2 / (mL^2)$ while L being the extension of the box trap.

The impurity density ρ_1^B shows a similar behavior as the majority component density (panel b1), also in terms of the role of the entanglement (panel b2). The width of ρ_r^{AB} shrinks with decreasing g_{AB} (panel d1), while the entanglement enhances the bunching between the two species (panel d2).

5. Quench Induced Tunneling Dynamics

Having analyzed in detail the ground state properties of our system, we subsequently study the dynamical response of a single impurity coupled to a lattice trapped species upon quenching the interspecies interaction strength g_{AB} . To this end we prepare the system in its ground state for $V = 500$, $g_{AB} = 6.0$ and $g_{AA} = 0.5$, leading to the formation of a two-fold degeneracy in the ground state and the two species phase separate [46]. In this sense, the ground state one-body density is given by a superposition state of two parity-symmetry broken configurations, where the density of the first one is depicted in Figure 10a and the second one corresponds to its parity-symmetric (with respect to $x = 0$) counterpart. It is possible to remove this degeneracy in order to select any of the states in the respective degenerate manifold. Technically, this is done by applying a small asymmetry, e.g., a tilt, to the lattice potential, thereby breaking the parity symmetry and energetically favoring one of the above-mentioned states [50].

To trigger the dynamics starting from the initial state configuration illustrated in Figure 10a we quench the interspecies interaction strength to a smaller value. As a representative example of the emergent tunneling dynamics of each species we present the temporal evolution of the corresponding one-body densities in Figure 10c,d following a quench to $g_{AB} = 4.5$, while keeping fixed $V = 500$ and $g_{AA} = 0.5$. In this case the impurity performs an oscillatory motion which is reminiscent of the tunneling of a particle in a double-well. This can be attributed to the lifting of the degeneracy for smaller interspecies interaction strengths. For a post-quench value of $g_{AB} = 4.5$ the initially prepared state has a substantial overlap with the post-quench ground state and the first excited state such that in the course of the dynamics the system will oscillate between those two. This is similar to a single particle in a double-well which is prepared as a superposition of the

first doublet and undergoes a tunneling between the sites. Correspondingly, the majority species will undergo a collective tunneling in the lattice geometry [50,53]. Thus, the probability distribution of a single majority species particle will oscillate between the initial distribution Figure 10a and its parity-symmetric counterpart. Due to the repulsive nature of the interspecies coupling the two species move in opposite directions such that they end up in phase-separated configurations after half a period. Note that the oscillation period, being the energy gap between the two energetically lowest eigenstates of the post-quench Hamiltonian (not shown here), depends on the post-quench g_{AB} . This can be easily verified by monitoring the temporal evolution of the averaged position of the impurity [13] which is defined as

$$\langle \hat{X}_B \rangle = \int_{-L/2}^{L/2} dx \rho_1^B(x)x. \tag{11}$$

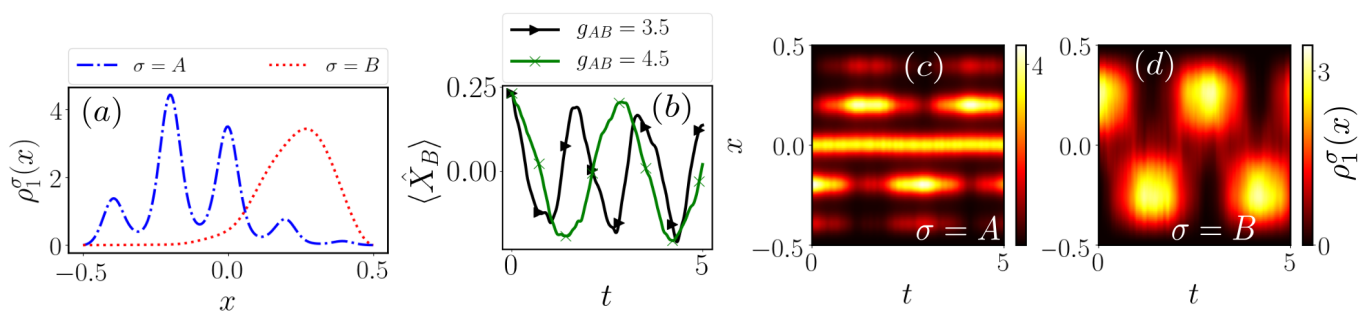


Figure 10. (a) One-body density $\rho_1^\sigma(x)$ of the initial state configuration for $V = 500$, $g_{AA} = 0.5$ and $g_{AB} = 6.0$ at $t = 0$. Temporal evolution of (b) the averaged position of the impurity $\langle \hat{X}_B \rangle$ (see Equation (11)), (c) the one-body density of the majority species and (d) the one-body density of the impurity upon quenching the interspecies interaction strength to $g_{AB} = 4.5$.

For various post-quench g_{AB} we find that the impurity will occupy its parity-symmetric counterpart, reflected in the decrease of $\langle \hat{X}_B \rangle$ towards negative values, while the oscillation decreases with smaller g_{AB} Figure 10b.

In order to gain insight into beyond mean-field effects we investigate the natural populations n_j^σ (see Equation (8)) which indicate the degree of fragmentation of the subsystem [9,71]. For simplicity here we present the populations of the first two dominantly populated natural orbitals while using six orbitals in the actual calculations. The initial depletion of both subsystems is rather small, i.e., $n_1^A \approx 0.996$ and $n_1^B \approx 0.99$, such that any decrease of these populations upon quenching g_{AB} is due to dynamical many-body effects. We find that for both subsystems dominantly two natural orbitals contribute during the dynamics Figure 11c,d, while the ones of the medium are less impacted by the quench. For the natural populations of the impurity signatures of an oscillation can be observed, where n_1^B initially decreases and revives back towards $n_1^B \approx 0.99$, while n_2^B initially increases and afterwards drops back to nearly zero. In order to attribute the occupation of the additional natural orbital to physical processes, we analyze the spatial distribution of the natural orbitals $\Phi_j^B(x, t)$ (see Equation (8)) themselves focusing on the impurity Figure 11a,b. In Figure 11a we observe that the first natural orbital corresponds to the oscillatory behavior of the one-body density of the impurity, but lacking the smooth transition between the phase-separated configurations (see Figure 10d). The first natural orbital dominates during the dynamics and we can interpret its behavior as corresponding to the presence of the phase-separated density configurations. Consequently, the second natural orbital Figure 11b, resembling the mirror image of the first one, contributes to deviations from this solution. Due to its structure we can deduce that it is responsible for initiating the transport of the impurity, thereby allowing for the counterflow of the two species. Note that the presence of more than one natural orbital during the dynamics is a clear signature that mean-field theory would not provide an accurate description of the system dynamics.

Hence, the fact that $|\Phi_2^B\rangle$ is occupied is a manifestation of many-body effects, influencing the motion of both species.

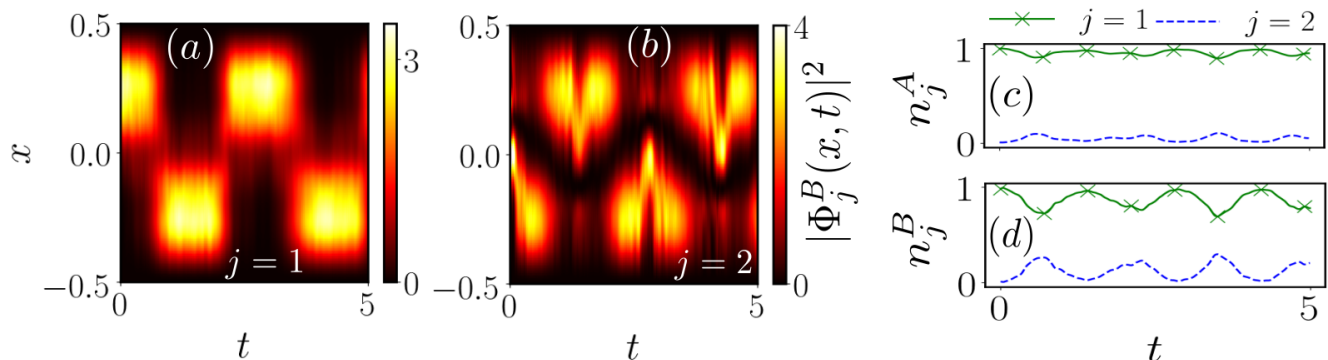


Figure 11. Temporal evolution of the density of (a) the first and (b) the second natural orbital $\Phi_j^B(x, t)$ (see Equation (8)) of the impurity and (c), (d) the natural populations n_j^σ of both subsystems upon quenching the interspecies interaction strength g_{AB} of the ground state in Figure 10a to $g_{AB} = 4.5$.

6. Summary and Outlook

In this work we analyze the static and dynamical properties of a few-body particle-imbalanced bosonic mixture at zero temperature. Importantly, the components are exposed to different one-dimensional external traps where the majority species is subject to a finite lattice potential while the single impurity is trapped in a box of the same extension as the lattice. We study the response of the composite system upon the variation of majority-impurity coupling g_{AB} and majority component internal parameters being either the lattice depth V or the majority-majority interaction strength g_{AA} .

To quantify the response of static properties we employ the fidelity between two density operators describing ground states at zero and a finite intercomponent interaction g_{AB} . We contrast the response at the many-body to the single-particle level. We observe that the composite system is quite robust to the variation of the intercomponent interaction at strongly repulsive g_{AA} , while being fragile at strongly attractive g_{AB} and deep lattices V as well as when g_{AA} is weakly attractive and g_{AB} is strongly attractive. Upon comparison to the fidelities between the corresponding reduced one-body density operators of each component, we not only observe that each species is affected to a much smaller degree, but they also respond differently. Thus, for the impurity atom the deviation from the box ground state increases smoothly with increasing absolute value of g_{AB} , while the reduced density of the majority component remains very robust to g_{AB} variations except for the above mentioned parameter regions where the many-body fidelity exhibits significant structural changes in the ground state.

Next, we have been performing a further classification of our system based on entropy measures. Namely, we quantify the amount of entanglement and intraspecies correlations deposited in the binary mixture by evaluating the von Neumann entropy of the respective subsystems. Interestingly, we find that our composite system is only weakly entangled for parameter regions which undergo substantial structural changes. Additionally, we observe that while the entanglement entropy continuously grows with increasing repulsive g_{AB} , it does not behave the same for attractive g_{AB} , where it reaches a local maximum at a finite value of $g_{AB} < 0$. Another peculiar observation is that the fragmentation entropy of the majority component undergoes a strong variation for parameter regions, where the fidelity measure does not show any evidence of majority particles being affected by the intercomponent interaction. Even though the mixed character of the reduced density of the medium suffers from substantial changes, it remains un-observable on the single-particle level.

To visualize our observations stemming from the fidelity measure we show the one-body density distributions of each component along with the probability distributions

for two particles of the same or different species to be measured at a relative distance from each other. These quantities are usually accessible in state-of-the-art ultracold atom experiments and determine the expectation values of local one- and two-body observables. Indeed, strong deviations appearing in the fidelity at the single-particle level are also clearly visible in the corresponding one-body density. At positive couplings we observe an interspecies phase separation where the impurity is pushed to the box edges, while leaving the majority component intact. At negative couplings both components tend to increase their localization at the central well.

To further quantify our conclusions stemming from the entanglement measure we rely on the difference between the above probability distributions and the corresponding ones when assuming a disentangled state in our calculations. Again, we find strong deviations for parameters displaying high entanglement entropy values. Thus, at positive couplings the entanglement favors the process of phase separation, while at negative couplings it generally, but not always, counteracts the localization of both species.

Quenching the interspecies interaction strength we are able to induce a dynamical process which for the impurity is reminiscent of the tunneling of a single particle in a double well potential. This can be attributed to the lifting of the degeneracy for the corresponding post-quench Hamiltonian as well as the substantial overlap of the initial state configuration with the post-quench ground state and the first excited state. Due to the repulsive interspecies interaction also the majority species will undergo a tunneling in the lattice geometry such that the two species move in opposite directions, ending up in phase-separated configurations after half a period. We identify the presence of two dominant natural orbitals for the impurity species during the dynamics, where the first one corresponds to phase-separated configurations in the respective one-body density, while the second one resembles the mirror image of the first one. The presence of an additional natural orbital emphasizes the many-body character of the dynamics, thereby influencing the motion of the impurity.

There are various promising research directions that are worth pursuing in the future. Indeed, the generalization of our findings for an increasing particle number in the medium or larger lattice potentials as well as the role of the lattice filling factor is desirable. Furthermore, a more elaborated analysis on the possibly emerging impurity-medium bound states or the engineering of droplet-like configurations in such settings at strong intercomponent attractions would be important. Furthermore, it would be intriguing to study the persistence and possible alterations of the identified spatial configurations in the presence of finite temperature which will impact the coherence of the lattice bosons [88–90]. Another perspective is to investigate the relevant radiofrequency spectrum [31,43] in order to capture the emergent polaron properties including their lifetime, residue and effective mass especially in the attractive interaction regimes of bound state formation.

Author Contributions: Conceptualization, M.P., K.K. and S.I.M.; Formal analysis, M.P. and K.K.; Investigation, M.P. and K.K.; Project administration, P.S.; Supervision, P.S.; Validation, P.S.; Visualization, M.P., K.K. and S.I.M.; Writing – original draft, M.P. and K.K.; Writing – review & editing, M.P., K.K. and S.I.M.

Funding: This research received no external funding.

Acknowledgments: M.P. and K.K. gratefully acknowledge a scholarship of the Studienstiftung des deutschen Volkes. S.I.M. gratefully acknowledges financial support in the framework of the Lenz-Ising Award of the Department of Physics of the University of Hamburg.

Conflicts of Interest: The authors declare no conflict of interest.

References

1. Bloch, I.; Dalibard, J.; Zwerger, W. Many-body physics with ultracold gases. *Rev. Mod. Phys.* **2008**, *80*, 885. [[CrossRef](#)]
2. Bloch, I. *Probing and Controlling Strongly Correlated Quantum Many-Body Systems Using Ultracold Quantum Gases*; Cambridge University Press: Cambridge, UK, 2017; p. 253.

3. Fukuhara, T.; Sugawa, S.; Takasu, Y.; Takahashi, Y. All-optical formation of quantum degenerate mixtures. *Phys. Rev. A* **2009**, *79*, 021601. [[CrossRef](#)]
4. Henderson, K.; Ryu, C.; MacCormick, C.; Boshier, M.G. Experimental demonstration of painting arbitrary and dynamic potentials for Bose–Einstein condensates. *New J. Phys.* **2009**, *11*, 043030. [[CrossRef](#)]
5. Serwane, F.; Zürn, G.; Lompe, T.; Ottenstein, T.; Wenz, A.; Jochim, S. Deterministic preparation of a tunable few-fermion system. *Science* **2011**, *332*, 336–338. [[CrossRef](#)] [[PubMed](#)]
6. Schmied, R.; Bancal, J.D.; Allard, B.; Fadel, M.; Scarani, V.; Treutlein, P.; Sangouard, N. Bell correlations in a Bose-Einstein condensate. *Science* **2016**, *352*, 441–444. [[CrossRef](#)]
7. Chin, C.; Grimm, R.; Julienne, P.; Tiesinga, E. Feshbach resonances in ultracold gases. *Rev. Mod. Phys.* **2010**, *82*, 1225. [[CrossRef](#)]
8. Köhler, T.; Góral, K.; Julienne, P.S. Production of cold molecules via magnetically tunable Feshbach resonances. *Rev. Mod. Phys.* **2006**, *78*, 1311. [[CrossRef](#)]
9. Mistakidis, S.I.; Katsimiga, G.C.; Kevrekidis, P.G.; Schmelcher, P. Correlation effects in the quench-induced phase separation dynamics of a two species ultracold quantum gas. *New J. Phys.* **2018**, *20*, 043052. [[CrossRef](#)]
10. Pyzh, M.; Schmelcher, P. Phase separation of a Bose-Bose mixture: Impact of the trap and particle-number imbalance. *Phys. Rev. A* **2020**, *102*, 023305. [[CrossRef](#)]
11. Petrov, D.S.; Astrakharchik, G.E. Ultradilute low-dimensional liquids. *Phys. Rev. Lett.* **2016**, *117*, 100401. [[CrossRef](#)]
12. Parisi, L.; Giorgini, S. Quantum droplets in one-dimensional Bose mixtures: a quantum Monte-Carlo study. *Phys. Rev. A* **2020**, *102*, 023318. [[CrossRef](#)]
13. Catani, J.; Lamporesi, G.; Naik, D.; Gring, M.; Inguscio, M.; Minardi, F.; Kantian, A.; Giamarchi, T. Quantum dynamics of impurities in a one-dimensional Bose gas. *Phys. Rev. A* **2012**, *85*, 023623. [[CrossRef](#)]
14. Meinert, F.; Knap, M.; Kirilov, E.; Jag-Lauber, K.; Zvonarev, M.B.; Demler, E.; Nägerl, H.C. Bloch oscillations in the absence of a lattice. *Science* **2017**, *356*, 945–948. [[CrossRef](#)]
15. Mistakidis, S.I.; Volosniev, A.G.; Zinner, N.T.; Schmelcher, P. Effective approach to impurity dynamics in one-dimensional trapped Bose gases. *Phys. Rev. A* **2019**, *100*, 013619. [[CrossRef](#)]
16. Ardila, L.P.; Giorgini, S. Impurity in a Bose-Einstein condensate: Study of the attractive and repulsive branch using quantum Monte Carlo methods. *Phys. Rev. A* **2015**, *92*, 033612. [[CrossRef](#)]
17. Grusdt, F.; Astrakharchik, G.E.; Demler, E. Bose polarons in ultracold atoms in one dimension: beyond the Fröhlich paradigm. *New J. Phys.* **2017**, *19*, 103035. [[CrossRef](#)]
18. Tajima, H.; Uchino, S. Many Fermi polarons at nonzero temperature. *New J. Phys.* **2018**, *20*, 073048. [[CrossRef](#)]
19. Dehkarghani, A.S.; Volosniev, A.G.; Zinner, N.T. Coalescence of two impurities in a trapped one-dimensional Bose gas. *Phys. Rev. Lett.* **2018**, *121*, 080405. [[CrossRef](#)]
20. Mistakidis, S.I.; Volosniev, A.G.; Schmelcher, P. Induced correlations between impurities in a one-dimensional quenched Bose gas. *Phys. Rev. Res.* **2020**, *2*, 023154. [[CrossRef](#)]
21. Takahashi, J.; Tajima, H.; Nakano, E.; Iida, K. Extracting non-local inter-polaron interactions from collisional dynamics. *arXiv* **2020**, arXiv:2011.07911.
22. Brauneis, F.; Hammer, H.W.; Leshchko, M.; Volosniev, A.G. Impurities in a one-dimensional Bose gas: The flow equation approach. *arXiv* **2021**, arXiv:2101.10958.
23. Massignan, P.; Zaccanti, M.; Bruun, G.M. Polarons, dressed molecules and itinerant ferromagnetism in ultracold Fermi gases. *Rep. Progr. Phys.* **2014**, *77*, 034401. [[CrossRef](#)]
24. Schmidt, R.; Knap, M.; Ivanov, D.A.; You, J.S.; Cetina, M.; Demler, E. Universal many-body response of heavy impurities coupled to a Fermi sea: a review of recent progress. *Rep. Progr. Phys.* **2018**, *81*, 024401. [[CrossRef](#)]
25. Fukuhara, T.; Kantian, A.; Endres, M.; Cheneau, M.; Schauss, P.; Hild, S.; Bellem, D.; Schollwöck, U.; Giamarchi, T.; Gross, C.; et al. Quantum dynamics of a mobile spin impurity. *Nat. Phys.* **2013**, *9*, 235–241. [[CrossRef](#)]
26. Yan, Z.Z.; Ni, Y.; Robens, C.; Zwierlein, M.W. Bose polarons near quantum criticality. *Science* **2020**, *368*, 190–194. [[CrossRef](#)] [[PubMed](#)]
27. Scazza, F.; Valtolina, G.; Massignan, P.; Recati, A.; Amico, A.; Burchianti, A.; Fort, C.; Inguscio, M.; Zaccanti, M.; Roati, G. Repulsive Fermi polarons in a resonant mixture of ultracold Li 6 atoms. *Phys. Rev. Lett.* **2017**, *118*, 083602. [[CrossRef](#)] [[PubMed](#)]
28. Jørgensen, N.B.; Wacker, L.; Skalmstang, K.T.; Parish, M.M.; Levinsen, J.; Christensen, R.S.; Bruun, G.M.; Arlt, J.J. Observation of attractive and repulsive polarons in a Bose-Einstein condensate. *Phys. Rev. Lett.* **2016**, *117*, 055302. [[CrossRef](#)]
29. Cetina, M.; Jag, M.; Lous, R.S.; Fritsche, I.; Walraven, J.T.; Grimm, R.; Levinsen, J.; Parish, M.M.; Schmidt, R.; Knap, M.; et al. Ultrafast many-body interferometry of impurities coupled to a Fermi sea. *Science* **2016**, *354*, 96–99. [[CrossRef](#)]
30. Wenz, A.; Zürn, G.; Murmann, S.; Brouzos, I.; Lompe, T.; Jochim, S. From few to many: Observing the formation of a Fermi sea one atom at a time. *Science* **2013**, *342*, 457–460. [[CrossRef](#)]
31. Mistakidis, S.I.; Koutentakis, G.M.; Grusdt, F.; Sadeghpour, H.R.; Schmelcher, P. Radiofrequency spectroscopy of one-dimensional trapped Bose polarons: crossover from the adiabatic to the diabatic regime. *arXiv* **2020**, arXiv:2011.13756.
32. Mistakidis, S.I.; Koutentakis, G.M.; Katsimiga, G.C.; Busch, T.; Schmelcher, P. Many-body quantum dynamics and induced correlations of Bose polarons. *New J. Phys.* **2020**, *22*, 043007. [[CrossRef](#)]
33. Boudjemâa, A.; Guebli, N.; Sekmane, M.; Khelifa-Karfa, S. Breathing modes of repulsive polarons in Bose–Bose mixtures. *J. Phys. Cond. Matt.* **2020**, *32*, 415401. [[CrossRef](#)]

34. Ardila, L.A.P.; Astrakharchik, G.E.; Giorgini, S. Strong coupling Bose polarons in a two-dimensional gas. *Phys. Rev. Res.* **2020**, *2*, 023405. [[CrossRef](#)]
35. Camacho-Guardian, A.; Ardila, L.A.P.; Pohl, T.; Bruun, G.M. Bipolarons in a Bose-Einstein condensate. *Phys. Rev. Lett.* **2018**, *121*, 013401. [[CrossRef](#)] [[PubMed](#)]
36. Mukherjee, K.; Mistakidis, S.I.; Majumder, S.; Schmelcher, P. Induced interactions and quench dynamics of bosonic impurities immersed in a Fermi sea. *Phys. Rev. A* **2020**, *102*, 053317. [[CrossRef](#)]
37. Bougas, G.; Mistakidis, S.I.; Schmelcher, P. Pattern formation of correlated impurities subjected to an impurity-medium interaction pulse. *Phys. Rev. A* **2021**, *103*, 023313. [[CrossRef](#)]
38. Tajima, H.; Takahashi, J.; Nakano, E.; Iida, K. Collisional dynamics of polaronic clouds immersed in a Fermi sea. *Phys. Rev. A* **2020**, *102*, 051302. [[CrossRef](#)]
39. Tonielli, F.; Chakraborty, N.; Grusdt, F.; Marino, J. Ramsey interferometry of non-Hermitian quantum impurities. *Phys. Rev. Res.* **2020**, *2*, 032003. [[CrossRef](#)]
40. Mistakidis, S.I.; Grusdt, F.; Koutentakis, G.M.; Schmelcher, P. Dissipative correlated dynamics of a moving impurity immersed in a Bose-Einstein condensate. *New J. Phys.* **2019**, *21*, 103026. [[CrossRef](#)]
41. Mukherjee, K.; Mistakidis, S.I.; Majumder, S.; Schmelcher, P. Pulse-and continuously driven many-body quantum dynamics of bosonic impurities in a Bose-Einstein condensate. *Phys. Rev. A* **2020**, *101*, 023615. [[CrossRef](#)]
42. Theel, F.; Keiler, K.; Mistakidis, S.I.; Schmelcher, P. Many-body collisional dynamics of impurities injected into a double-well trapped Bose-Einstein condensate. *arXiv* **2020**, arXiv:2009.12147.
43. Mistakidis, S.I.; Katsimiga, G.C.; Koutentakis, G.M.; Busch, T.; Schmelcher, P. Pump-probe spectroscopy of Bose polarons: Dynamical formation and coherence. *Phys. Rev. Res.* **2020**, *2*, 033380. [[CrossRef](#)]
44. Lausch, T.; Widera, A.; Fleischhauer, M. Prethermalization in the cooling dynamics of an impurity in a Bose-Einstein condensate. *Phys. Rev. A* **2018**, *97*, 023621. [[CrossRef](#)]
45. Palzer, S.; Zipkes, C.; Sias, C.; Köhl, M. Quantum transport through a Tonks-Girardeau gas. *Phys. Rev. Lett.* **2009**, *103*, 150601. [[CrossRef](#)]
46. Keiler, K.; Mistakidis, S.I.; Schmelcher, P. Doping a lattice-trapped bosonic species with impurities: From ground state properties to correlated tunneling dynamics. *New J. Phys.* **2020**, *22*, 083003. [[CrossRef](#)]
47. Bohrdt, A.; Grusdt, F.; Knap, M. Dynamical formation of a magnetic polaron in a two-dimensional quantum antiferromagnet. *New J. Phys.* **2020**, *22*, 123023. [[CrossRef](#)]
48. Cai, Z.; Wang, L.; Xie, X.; Wang, Y. Interaction-induced anomalous transport behavior in one-dimensional optical lattices. *Phys. Rev. A* **2010**, *81*, 043602. [[CrossRef](#)]
49. Johnson, T.H.; Clark, S.R.; Bruderer, M.; Jaksch, D. Impurity transport through a strongly interacting bosonic quantum gas. *Phys. Rev. A* **2011**, *84*, 023617. [[CrossRef](#)]
50. Theel, F.; Keiler, K.; Mistakidis, S.I.; Schmelcher, P. Entanglement-assisted tunneling dynamics of impurities in a double well immersed in a bath of lattice trapped bosons. *New J. Phys.* **2020**, *22*, 023027. [[CrossRef](#)]
51. Keiler, K.; Schmelcher, P. State engineering of impurities in a lattice by coupling to a Bose gas. *New J. Phys.* **2018**, *20*, 103042. [[CrossRef](#)]
52. Keiler, K.; Krönke, S.; Schmelcher, P. Correlation induced localization of lattice trapped bosons coupled to a Bose-Einstein condensate. *New J. Phys.* **2018**, *20*, 033030. [[CrossRef](#)]
53. Keiler, K.; Schmelcher, P. Interaction-induced single-impurity tunneling in a binary mixture of trapped ultracold bosons. *Phys. Rev. A* **2019**, *100*, 043616. [[CrossRef](#)]
54. Bruderer, M.; Bao, W.; Jaksch, D. Self-trapping of impurities in Bose-Einstein condensates: Strong attractive and repulsive coupling. *Europhys. Lett.* **2008**, *82*, 30004. [[CrossRef](#)]
55. Yin, T.; Cocks, D.; Hofstetter, W. Polaronic effects in one-and two-band quantum systems. *Phys. Rev. A* **2015**, *92*, 063635. [[CrossRef](#)]
56. Grusdt, F.; Shashi, A.; Abanin, D.; Demler, E. Bloch oscillations of bosonic lattice polarons. *Phys. Rev. A* **2014**, *90*, 063610. [[CrossRef](#)]
57. Weber, C.; John, S.; Spethmann, N.; Meschede, D.; Widera, A. Single Cs atoms as collisional probes in a large Rb magneto-optical trap. *Phys. Rev. A* **2010**, *82*, 042722. [[CrossRef](#)]
58. Will, S.; Best, T.; Braun, S.; Schneider, U.; Bloch, I. Coherent Interaction of a Single Fermion with a Small Bosonic Field. *Phys. Rev. Lett.* **2011**, *106*, 115305. [[CrossRef](#)] [[PubMed](#)]
59. Tajima, H.; Takahashi, J.; Mistakidis, S.I.; Nakano, E.; Iida, K. Polaron problems in ultracold atoms: Role of the medium across different spatial dimensions. *arXiv* **2021**, arXiv:2101.07643.
60. Cao, L.; Bolsinger, V.; Mistakidis, S.; Koutentakis, G.; Krönke, S.; Schurer, J.; Schmelcher, P. A unified ab initio approach to the correlated quantum dynamics of ultracold fermionic and bosonic mixtures. *J. Chem. Phys.* **2017**, *147*, 044106. [[CrossRef](#)] [[PubMed](#)]
61. Cao, L.; Krönke, S.; Vendrell, O.; Schmelcher, P. The multi-layer multi-configuration time-dependent Hartree method for bosons: Theory, implementation, and applications. *J. Chem. Phys.* **2013**, *139*, 134103. [[CrossRef](#)]
62. Krönke, S.; Cao, L.; Vendrell, O.; Schmelcher, P. Non-equilibrium quantum dynamics of ultra-cold atomic mixtures: The multi-layer multi-configuration time-dependent Hartree method for bosons. *New J. Phys.* **2013**, *15*, 063018. [[CrossRef](#)]

63. Mistakidis, S.I.; Katsimiga, G.C.; Koutentakis, G.M.; Busch, T.; Schmelcher, P. Quench dynamics and orthogonality catastrophe of Bose polarons. *Phys. Rev. Lett.* **2019**, *122*, 183001. [[CrossRef](#)]
64. Pflanzner, A.C.; Zöllner, S.; Schmelcher, P. Material-barrier tunnelling in one-dimensional few-boson mixtures. *J. Phys. B At. Mol. Opt. Phys.* **2009**, *42*, 231002. [[CrossRef](#)]
65. Myatt, C.J.; Burt, E.A.; Ghrist, R.W.; Cornell, E.A.; Wieman, C.E. Production of Two Overlapping Bose-Einstein Condensates by Sympathetic Cooling. *Phys. Rev. Lett.* **1997**, *78*, 586–589. [[CrossRef](#)]
66. Hall, D.S.; Matthews, M.R.; Ensher, J.R.; Wieman, C.E.; Cornell, E.A. Dynamics of Component Separation in a Binary Mixture of Bose-Einstein Condensates. *Phys. Rev. Lett.* **1998**, *81*, 1539–1542. [[CrossRef](#)]
67. Miesner, H.J.; Stamper-Kurn, D.M.; Stenger, J.; Inouye, S.; Chikkatur, A.P.; Ketterle, W. Observation of Metastable States in Spinor Bose-Einstein Condensates. *Phys. Rev. Lett.* **1999**, *82*, 2228–2231. [[CrossRef](#)]
68. Maddaloni, P.; Modugno, M.; Fort, C.; Minardi, F.; Inguscio, M. Collective Oscillations of Two Colliding Bose-Einstein Condensates. *Phys. Rev. Lett.* **2000**, *85*, 2413–2417. [[CrossRef](#)]
69. Mertes, K.M.; Merrill, J.W.; Carretero-González, R.; Frantzeskakis, D.J.; Kevrekidis, P.G.; Hall, D.S. Nonequilibrium Dynamics and Superfluid Ring Excitations in Binary Bose-Einstein Condensates. *Phys. Rev. Lett.* **2007**, *99*, 190402. [[CrossRef](#)]
70. Becker, C.; Stellmer, S.; Soltan-Panahi, P.; Dörscher, S.; Baumert, M.; Richter, E.M.; Kronjäger, J.; Bongs, K.; Sengstock, K. Oscillations and interactions of dark and dark-bright solitons in Bose-Einstein condensates. *Nat. Phys.* **2008**, *4*, 496–501. [[CrossRef](#)]
71. Lode, A.U.J.; Lévêque, C.; Madsen, L.B.; Streltsov, A.I.; Alon, O.E. Colloquium: Multiconfigurational time-dependent Hartree approaches for indistinguishable particles. *Rev. Mod. Phys.* **2020**, *92*, 011001. [[CrossRef](#)]
72. Alon, O.E.; Beinke, R.; Cederbaum, L.S. Many-body effects in the excitations and dynamics of trapped Bose-Einstein condensates. *arXiv* **2021**, arXiv:2101.11615.
73. Horodecki, R.; Horodecki, P.; Horodecki, M.; Horodecki, K. Quantum entanglement. *Rev. Mod. Phys.* **2009**, *81*, 865. [[CrossRef](#)]
74. Light, J.; Hamilton, I.; Lill, J. Generalized discrete variable approximation in quantum mechanics. *J. Chem. Phys.* **1985**, *82*, 1400–1409. [[CrossRef](#)]
75. Raab, A. On the Dirac-Frenkel/McLachlan variational principle. *Chem. Phys. Lett.* **2000**, *319*, 674–678. [[CrossRef](#)]
76. Jozsa, R. Fidelity for mixed quantum states. *J. Mod. Opt.* **1994**, *41*, 2315–2323. [[CrossRef](#)]
77. Wang, W.; Penna, V.; Capogrosso-Sansone, B. Inter-species entanglement of Bose-Bose mixtures trapped in optical lattices. *New J. Phys.* **2016**, *18*, 063002. [[CrossRef](#)]
78. Bengtsson, I.; Życzkowski, K. *Geometry of Quantum States: An Introduction to Quantum Entanglement*; Cambridge University Press: Cambridge, UK, 2017.
79. Roy, R.; Gammal, A.; Tsatsos, M.C.; Chatterjee, B.; Chakrabarti, B.; Lode, A.U.J. Phases, many-body entropy measures, and coherence of interacting bosons in optical lattices. *Phys. Rev. A* **2018**, *97*, 043625. [[CrossRef](#)]
80. Bera, S.; Haldar, S.K.; Chakrabarti, B.; Trombettoni, A.; Kota, V.K.B. Relaxation of Shannon entropy for trapped interacting bosons with dipolar interactions. *Eur. Phys. J. D* **2020**, *74*, 1–10. [[CrossRef](#)]
81. Penna, V.; Richaud, A. The phase-separation mechanism of a binary mixture in a ring trimer. *Sci. Rep.* **2018**, *8*, 10242. [[CrossRef](#)]
82. Richaud, A.; Penna, V. Pathway toward the formation of supermixed states in ultracold boson mixtures loaded in ring lattices. *Phys. Rev. A* **2019**, *100*, 013609. [[CrossRef](#)]
83. Bakr, W.S.; Peng, A.; Tai, M.E.; Ma, R.; Simon, J.; Gillen, J.I.; Fölling, S.; Pollet, L.; Greiner, M. Probing the superfluid-to-Mott insulator transition at the single-atom level. *Science* **2010**, *329*, 547–550. [[CrossRef](#)]
84. Sherson, J.F.; Weitenberg, C.; Endres, M.; Cheneau, M.; Bloch, I.; Kuhr, S. Single-atom-resolved fluorescence imaging of an atomic Mott insulator. *Nature* **2010**, *467*, 68–72. [[CrossRef](#)] [[PubMed](#)]
85. Omran, A.; Boll, M.; Hilker, T.A.; Kleinlein, K.; Salomon, G.; Bloch, I.; Gross, C. Microscopic Observation of Pauli Blocking in Degenerate Fermionic Lattice Gases. *Phys. Rev. Lett.* **2015**, *115*, 263001. [[CrossRef](#)] [[PubMed](#)]
86. Hohmann, M.; Kindermann, F.; Lausch, T.; Mayer, D.; Schmidt, F.; Lutz, E.; Widera, A. Individual Tracer Atoms in an Ultracold Dilute Gas. *Phys. Rev. Lett.* **2017**, *118*, 263401. [[CrossRef](#)]
87. Pyzh, M.; Krönke, S.; Weitenberg, C.; Schmelcher, P. Quantum point spread function for imaging trapped few-body systems with a quantum gas microscope. *New J. Phys.* **2019**, *21*, 053013. [[CrossRef](#)]
88. Lingua, F.; Capogrosso-Sansone, B.; Minardi, F.; Penna, V. Thermometry of bosonic mixtures in Optical Lattices via Demixing. *Sci. Rep.* **2017**, *7*, 1–9. [[CrossRef](#)]
89. Suthar, K.; Angom, D. Characteristic temperature for the immiscible-miscible transition of binary condensates in optical lattices. *Phys. Rev. A* **2017**, *95*, 043602. [[CrossRef](#)]
90. Suthar, K.; Angom, D. Optical-lattice-influenced geometry of quasi-two-dimensional binary condensates and quasiparticle spectra. *Phys. Rev. A* **2016**, *93*, 063608. [[CrossRef](#)]